Applied Catalysis B: Environmental 338 (2023) 123012

Contents lists available at ScienceDirect

Applied Catalysis B: Environmental

journal homepage: www.elsevier.com/locate/apcatb

Gold nanoparticles supported on $ZnGa_2O_4$ nanosheets as efficient photocatalysts for selective oxidation of methane to ethane under ambient conditions

Yao Chai [1], Sishi Tang [1], Qiang Wang, Qiong Wu, Jun Liang [*], Li Li [*]

State Key Laboratory of High-efficiency Utilization of Coal and Green Chemical Engineering, College of Chemistry and Chemical Engineering, Ningxia University, Yinchuan 750021, PR China

ARTICLE INFO

Keywords:
Gold nanoparticles
$ZnGa_2O_4$ nanosheets
Oxidative coupling of methane
Superoxide ions
Photocatalytic

ABSTRACT

In this study, we fabricated photocatalysts comprising of $ZnGa_2O_4$ nanosheets modified with gold (Au) nanoparticles for the selective oxidative coupling of methane (CH_4). Our findings indicate that the C_2H_6 production rate of $ZnGa_2O_4$ with the optimal loading of Au nanoparticles (NPs) reached 1315.3 μmol g^{-1} h^{-1}, with a selectivity of 53 %. These results were considerably higher than those obtained with pure $ZnGa_2O_4$. The presence of Au NPs facilitated the activation of O_2 molecules, leading to the generation of superoxide ions (O_2^-), which were the primary active species responsible for the cleavage of CH_4 into methyl radicals ($\bullet CH_3$). Additionally, Au NPs stabilized $\bullet CH_3$ and promoted the coupling of $\bullet CH_3$ into C_2H_6 while impeding the excessive oxidation of $\bullet CH_3$ into CO_2. In conclusion, our study demonstrates that modifying $ZnGa_2O_4$ with Au NPs can significantly enhance the yield and selectivity of C_2H_6 during the photocatalytic oxidative coupling of CH_4.

1. Introduction

The catalytic conversion of CH_4 into valuable chemicals is an essential research direction in the field of C1 catalysis [1–3]. Traditionally, thermal catalytic pathways have been used to convert CH_4 into high-value compounds such as CH_3OH, C_2H_6, C_2H_4, etc [4–6]. However, these pathways require high catalytic reaction temperatures (700–1110 °C) and high reaction pressures (> 1 MPa). Additionally, as the reaction proceeds, catalyst deactivation due to carbon deposition and the occurrence of side reactions such as CH_4 transition oxidation inevitably occur [7–9]. Therefore, the development of mild, green, low-energy, and low-cost CH_4 conversion routes has become a key challenge in the field. By exploring alternative catalytic pathways, we can overcome these limitations and develop more efficient and sustainable methods for CH_4 conversion.

Fortunately, the use of inorganic semiconductor photocatalysts for the photocatalytic conversion of CH_4 into high-value products has emerged as a promising direction for green CH_4 transformation and has gained significant attention [10]. A range of noble metal-loaded semiconductor photocatalysts have been developed and reported, including Au-ZnO/TiO_2 hybrid materials, Au/ZnO porous nanosheets, and Pd atom-modified TiO_2 materials [11–13]. These photocatalysts have been shown to achieve high efficiency in oxidative or non-oxidative coupling of CH_4 under illumination conditions. It is worth noting that the photocatalytic non-oxidative coupling of CH_4 is an endothermic reaction, which is limited by thermodynamics and can be challenging to achieve high conversion rates [11]. In contrast, CH_4 oxidative coupling is an exothermic reaction, which makes it more thermodynamically favorable and can achieve higher conversion rates than non-oxidative coupling [11]. Therefore, oxidative coupling may be the preferred reaction pathway for achieving the highest CH_4 conversion rates.

The photocatalytic oxidative coupling of CH_4 involves the dehydrogenation of CH_4 molecules on the catalyst surface to produce $\bullet CH_3$, which then couples into C_2H_6 molecules, making it a recognized pathway for CH_4 conversion [14–16]. However, the main challenge of this reaction is the adsorption and activation of CH_4 molecules to promote dehydrogenation to generate $\bullet CH_3$, and stabilizing $\bullet CH_3$ to prevent its transitional oxidation to CO_2 by O_2 [17,18]. To overcome this challenge, constructing an efficient active center for CH_4 adsorption and activation has become a focus of research. Noble metal nanoparticles have been shown to efficiently stabilize $\bullet CH_3$ and facilitate its coupling into C_2H_6, making them effective catalysts for this reaction [19].

* Corresponding authors.
E-mail addresses: junliang@nxu.edu.cn (J. Liang), li_l@nxu.edu.cn (L. Li).
[1] ‡Yao Chai and Sishi Tang contributed equally.

https://doi.org/10.1016/j.apcatb.2023.123012
Received 6 April 2023; Received in revised form 13 June 2023; Accepted 16 June 2023
Available online 17 June 2023

Reactive oxygen species play a crucial role in promoting the generation of $\bullet CH_3$ from CH_4, and are generally formed by photogenerated holes oxidizing lattice oxygen or adsorbing oxygen on the surface [20]. Therefore, noble metal modification and efficient generation of reactive oxygen species have become the basic requirements for developing efficient catalysts for CH_4 oxidative coupling.

Here, we have successfully designed and synthesized a photocatalyst for methane oxidative coupling reaction by modifying $ZnGa_2O_4$ nanosheets with Au NPs. Our optimized catalyst showed a remarkable C_2H_6 yield of 1315.3 μmol g^{-1} h^{-1} with a selectivity of 53 %. Our findings suggest that Au NPs play a crucial role in activating O_2 molecules, which leads to the generation of O_2^-. This O_2^- species is the main active substance responsible for the splitting of CH_4 into $\bullet CH_3$. Our results also revealed that the Au NPs can stabilize $\bullet CH_3$ and promote its coupling into C_2H_6 while simultaneously inhibiting its excessive oxidation into CO_2. Our study highlights the importance of Au modification in enhancing the photocatalytic activity of $ZnGa_2O_4$ nanosheets for CH_4 conversion.

2. Experimental section

2.1. Preparation of Au-$ZnGa_2O_4$

After 0.42 g of PVP was dissolved in 32 mL of deionized water, 0.1 g of $ZnGa_2O_4$ was weighed and added to the above solution, stirred, and dispersed. Then a particular volume of $HAuCl_4{\cdot}4H_2O$ solution (2 mg/mL) was added and stirred for 40 min. Finally, 0.48 g of $C_6H_8O_6$ was dissolved in 16 mL of deionized water, and the solution was slowly dropped into the above-mixed solution, and the mixture was stirred continuously for 3 h in a water bath at 88 °C. Once the reaction ended, the product was collected, washed with distilled water, and vacuum-dried at 40 °C for 6 h.

2.2. Photocatalytic activity measurement

10 mg of photocatalyst was uniformly dispersed in 1.5 mL of deionized water. Then, the dispersion liquid was put into a circular quartz tank with a diameter of 4 cm, and dried to form a film at 70 °C. The quartz tank containing the catalyst was placed in a 150 mL quartz batch reactor, sealed and evacuated to remove air from the reactor. After the air in the reactor was completely removed, 4 mL of pure CH4 gas and a certain volume of oxygen were injected with a chromatographic gas injection needle, respectively, and stirred for 1 h to reach the adsorption equilibrium. A 300 W xenon lamp (PLS-SXE300D/300DUV, Beijing Perfectlight Technology Co., Ltd.) was used as the light source (Fig. S1). After 3 h of illumination, 0.5 mL of gaseous product was removed from the reactor with a gas sampling needle, and the product was analyzed and quantified by gas chromatography with a flame ionization detector and a thermal conductivity detector (FULI GC9790II).

3. Results and discussion

3.1. Composition and Morphological Characterization

Fig. 1 outlines the catalyst preparation process. To create the $ZnGa_2O_4$ nanosheets photocatalyst, a simple solvothermal method was

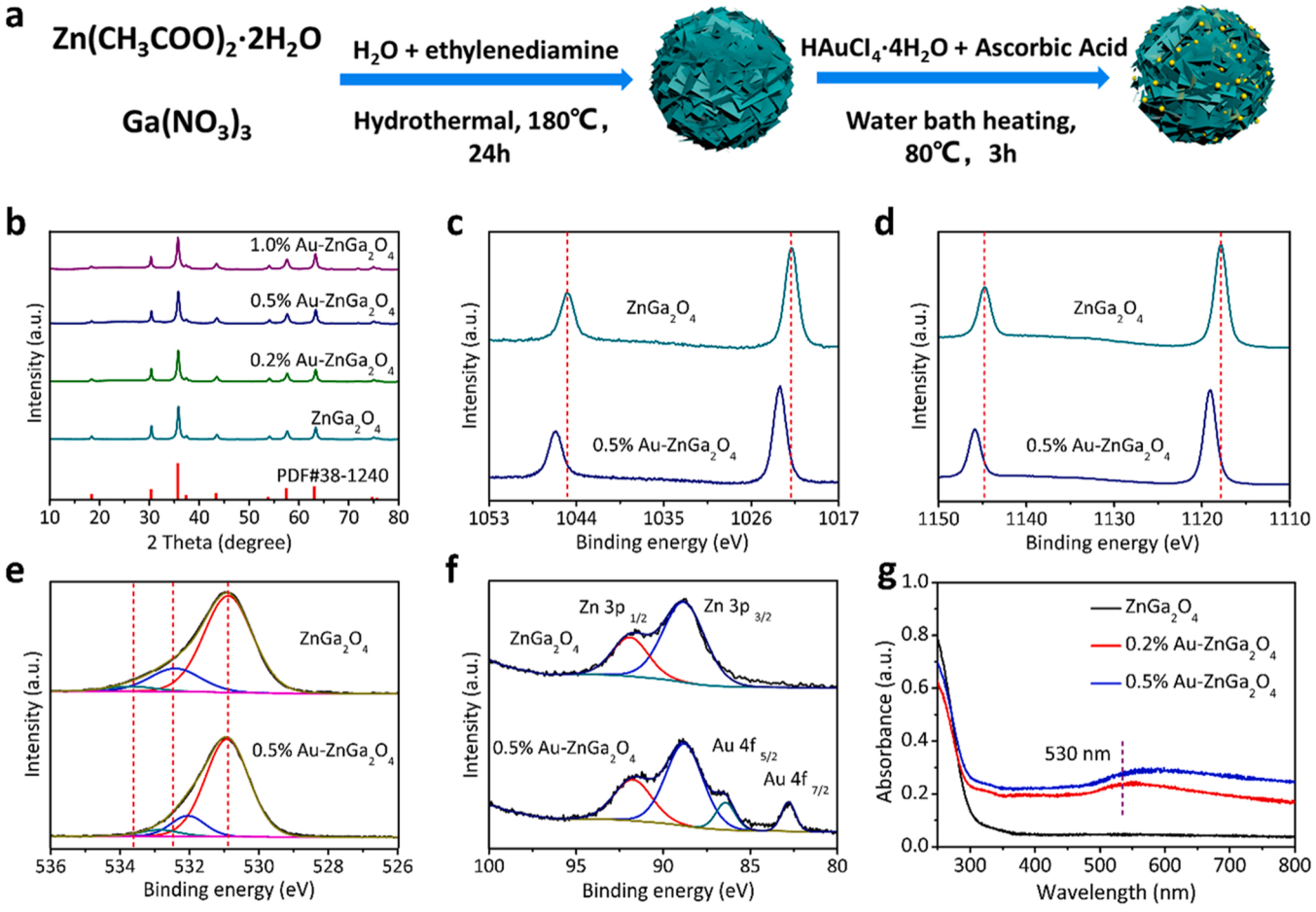

Fig. 1. (a) Schematic diagram of the preparation of Au-$ZnGa_2O_4$ composite photocatalyst. (b) XRD patterns of series of photocatalysts. XPS spectra of 0.5 % Au-$ZnGa_2O_4$ and $ZnGa_2O_4$: (c) Zn 3d, (d) Ga 2p, (e) O 1s, and (f) Zn 3p and Au 4f. (g) DRS patterns of 0.5 % Au-$ZnGa_2O_4$, 0.2 % Au-$ZnGa_2O_4$, and $ZnGa_2O_4$.

employed using a mixed solution of ethylenediamine and H_2O as the solvent [21]. The solution was then reduced with ascorbic acid as a reducing agent to obtain the $ZnGa_2O_4$ nanosheets photocatalyst supported by Au NPs (Fig. 1a). The crystal and electronic structures of the photocatalysts were analyzed using XRD and XPS, respectively. The XRD patterns of $ZnGa_2O_4$ and $ZnGa_2O_4$ loaded with different amounts of Au NPs in Fig. 1b corresponded to the standard cards of pure phase $ZnGa_2O_4$ (PDF#38–1240) with no other impurity diffraction peaks observed [22]. The XRD diffraction peaks of Au NPs were not observed, possibly due to their low content [23]. The doublets with binding energies of 1021.85 and 1044.95 eV in Fig. 1c were assigned to Zn^{2+} of $ZnGa_2O_4$ nanosheets. The binding energies of Zn^{2+} in the 0.5 % Au-$ZnGa_2O_4$ sample were shifted towards higher binding energy compared to pure $ZnGa_2O_4$, indicating electron transfer between Au NPs and $ZnGa_2O_4$ nanosheets [24]. Similarly, the binding energies of Ga^{3+} in the 0.5 % Au-$ZnGa_2O_4$ sample were also significantly shifted towards higher binding energy compared to pure $ZnGa_2O_4$ (Fig. 1d) [25]. The set of peaks with binding energies of 530.90, 532.45 and 533.61 eV were assigned to lattice oxygen, oxygen vacancies, and surface adsorbed oxygen species of $ZnGa_2O_4$ nanosheets, respectively (Fig. 1e) [26]. In the 0.5 % Au-$ZnGa_2O_4$ photocatalyst, the three peaks with binding energies of 530.93, 532.07, and 532.96 eV were assigned to lattice oxygen, oxygen vacancies, and surface adsorbed oxygen species [26,27]. The peaks with binding energies of 88.82 and 91.99 eV corresponded to Zn $3p_{1/2}$, and Zn $3p_{3/2}$ in both the $ZnGa_2O_4$ sample and the 0.5 % Au-ZnGa2O4 sample (Fig. 1f) [28]. The two peaks with binding energies of 82.79 and 86.44 eV corresponded to the Au $4f_{5/2}$ and Au $4f_{7/2}$ of the 0.5 % Au-$ZnGa_2O_4$, respectively [29]. The shifts in binding energies of the constituent elements of $ZnGa_2O_4$ indicate substantial charge transfer between Au NPs and $ZnGa_2O_4$, demonstrating a strong interaction between the two. UV-DRS spectra showed that the $ZnGa_2O_4$ and Au-$ZnGa_2O_4$ series samples had the same optical absorption band edge (~300 nm), corresponding to a band gap of 4.13 eV. With an increase in Au loading, the intensity of light absorption was significantly enhanced and accompanied by the appearance of Au plasmon resonance absorption at 530 nm (Fig. 1g) [30]. These results confirm that Au NPs are supported on the surface of $ZnGa_2O_4$, and there is a specific interaction mode between the two.

The microstructure of $ZnGa_2O_4$ modified with Au NPs was characterized using SEM and TEM. Fig. S2 shows SEM images of the 0.5 % Au-$ZnGa_2O_4$ sample at varying magnifications, which reveal that the sample exhibits the basic morphology of microflowers self-assembled from $ZnGa_2O_4$ two-dimensional nanosheets. However, the smaller size of the Au NPs makes their morphology difficult to observe. To address this, TEM images at different magnifications (Fig. 2a and b) were obtained, which confirmed that the Au NPs are dispersed on the $ZnGa_2O_4$ nanosheets and have an average size of ~10 nm. Additionally, high-resolution TEM (HRTEM) images (Fig. 2c–e) revealed two different lattice fringes of 0.251 and 0.235 nm, corresponding to $ZnGa_2O_4$ (3 1 1) and Au NPs (1 1 1) crystal faces, respectively [31,32]. It can be observed that Au NPs are closely attached to the surface of $ZnGa_2O_4$. Elemental mapping images (Fig. 2f–j) showed that the distribution of Au elements on the catalyst is uniform, confirming that the Au NPs are evenly distributed on the $ZnGa_2O_4$ surface. Furthermore, the specific surface areas of pure $ZnGa_2O_4$ and 0.5 % Au-$ZnGa_2O_4$ photocatalysts are 36.76 and 37.87 $cm^2\ g^{-1}$, respectively. The similarity in specific surface areas indicates that the difference in photocatalytic activity is not caused by the specific surface area (Fig. S3).

3.2. Photocatalytic CH_4 oxidative coupling

Fig. 3 depicts the photocatalytic activity of $ZnGa_2O_4$ and Au-modified $ZnGa_2O_4$ catalysts in the oxidative coupling reaction of CH_4. The study initially explores the effect of the amount of O_2 on the oxidative coupling of CH_4 (Fig. 3a). For the 0.5 % Au-$ZnGa_2O_4$ sample, the activity of the series products and their selectivity change with the increase of O_2 content. C_2H_6 selectivity decreases, while the activity of CO_2 gradually increases. The appropriate amount of O_2 for the oxidative coupling of CH_4 is determined to be 1.6 mL, as it results in a C_2H_6 product yield of 1315.3 μmol g^{-1} h^{-1} and a selectivity of 53.3 %. Moreover, the disparity in the yields of H_2 and C_2H_6, with the H_2 yield being less than half of the expected ratio in the absence of O_2, indicates a

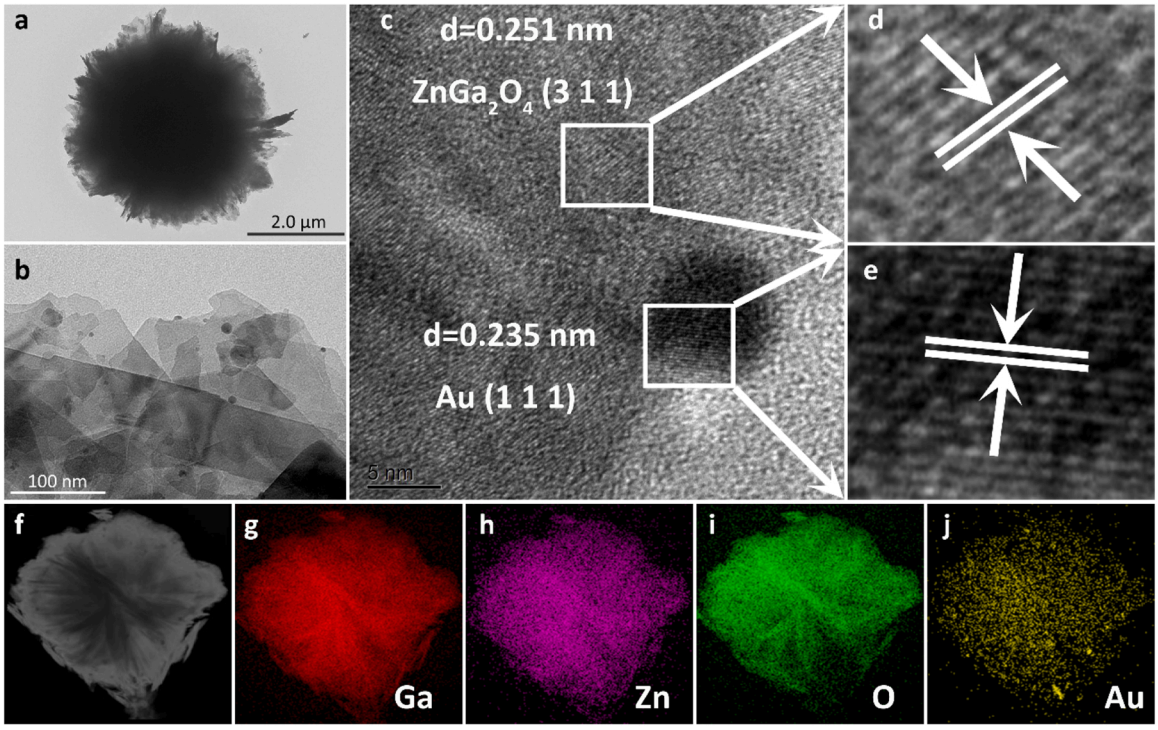

Fig. 2. . (a, b) TEM image of 0.5 % Au-$ZnGa_2O_4$ with a scale bar of 2.0 and 0.1 μm. (c) HRTEM image of 0.5 % Au-$ZnGa_2O_4$. (d, e) Enlarged view of different constituencies of HRTEM. (f–j) EDX elemental mapping images.

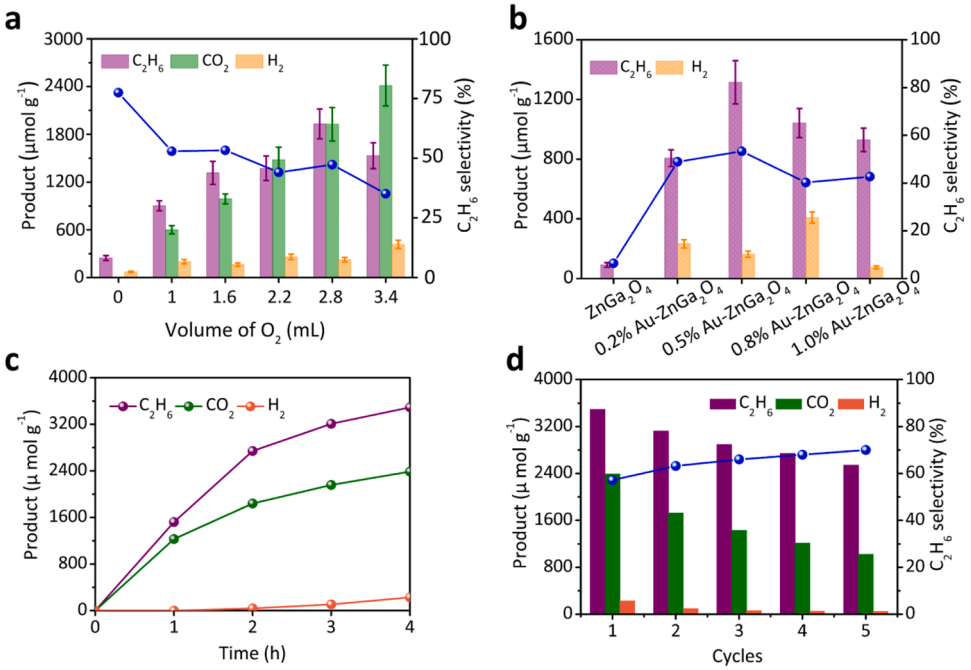

Fig. 3. Photocatalytic oxidative coupling of CH_4 performance. (a) Photocatalytic oxidative coupling of CH_4 activity of 0.5 % Au-$ZnGa_2O_4$ sample under different O_2 content. (b) Photocatalytic activity of oxidative coupling of CH_4 over $ZnGa_2O_4$ loaded with different amounts of Au. (c) Product activity as a function of reaction time, (d) Performance of C_2H_6, CO_2, and H_2 in durability tests.

deviation from the anticipated 1:1 stoichiometric ratio. This observation suggests the presence of other influencing factors or reactions that impact the distribution and yield of products in the absence of O_2. The use of batch reactors and the method of sample injection inevitably leads to oxygen leakage. When oxygen enters the reactor, it may react with hydrogen. Additionally, metal nanoparticles have a propensity for efficient hydrogen adsorption. Consequently, the adsorption of gold nanoparticles and the occurrence of oxygen leakage significantly contribute to the deviation in hydrogen gas yield. Fig. 3b displays the photocatalytic activity of $ZnGa_2O_4$ with different Au loadings for the oxidative coupling of CH_4. The formation rate of C_2H_6 exhibit a volcano-shaped relationship with increasing Au loading. Particularly, the 0.5 % Au-$ZnGa_2O_4$ sample achieves a C_2H_6 formation rate of 1315.3 μmol g^{-1} h^{-1} and a selectivity of 53.3 %, significantly higher than that of some common photocatalytic CH_4 coupling conversion systems (Table S1). However, the hydrogen production rate did not exhibit a consistent pattern with increasing Au NPs loading, suggesting the influence of factors or reactions other than Au NPs loading. The yield of hydrogen was affected by the adsorption of Au NPs and the occurrence of oxygen leakage, leading to bias. It is worth noting that in the CH_4 oxidative coupling reaction, the intermediate superoxide anion produced by O_2, as an oxidant, exhibits a strong oxidizing ability. As a result, CH_4 is directly oxidized to CO_2 in the absence of other oxygenates involved in CH_4 oxidation. The pure $ZnGa_2O_4$ sample has a C_2H_6 yield of only 91.04 μmol g^{-1} h^{-1}, while the CO_2 formation rate reaches 1329 μmol g^{-1} h^{-1}. In contrast, the CO_2 formation rate of the 0.5 % Au-$ZnGa_2O_4$ catalyst is 988 μmol g^{-1} h^{-1} (Fig. S4). The loading of Au, on the one hand, prevents the excessive oxidation of CH_4, and on the other hand, significantly enhances the C_2H_6 generation rate. Fig. 3c shows the dependence of the formation rate of CH_4 oxidative coupling products on the 0.5 % Au-$ZnGa_2O_4$ catalyst as a function of irradiation time. With an increase in irradiation time, the activity of the series of products continues to increase, but the growth rate decreases due to the consumption of O_2 in the reaction system. Several control experiments were performed to determine that the reaction is a light-induced CH_4 coupling reaction (Fig. S5). Without the addition of a catalyst or light, and with the use of Ar instead of CH_4, no related products are formed. The photocatalytic activity of oxidative coupling is much higher than that of non-oxidative coupling, indicating that the reaction is a photocatalytic oxidative coupling of the CH_4 reaction of the Au-$ZnGa_2O_4$ catalyst. Finally, Fig. 3d shows the stability test of the catalyst, which reveals that the activity of the product remains stable with an increase in the number of cycles. The XRD and DRS of the catalyst remain unchanged before and after the reaction, indicating that the catalyst has good cycling stability (Fig. S6 and Fig. S7).

3.3. Photoelectric and fluorescent characterization

To investigate the underlying factors contributing to the superior photocatalytic activity of the 0.5 % Au-$ZnGa_2O_4$ sample, we conducted photoelectrochemical and fluorescence spectroscopy analyses to evaluate the efficiency of photogenerated carrier separation and migration rates. The rapid separation efficiency and fast migration rate of photogenerated carriers often correspond to a high photocurrent density and a small electrochemical impedance radius, respectively [33]. Consistent with this expectation, the 0.5 % Au-$ZnGa_2O_4$ sample showed higher photocurrent density and smaller electrochemical impedance radius compared to pure $ZnGa_2O_4$, as depicted in Fig. 4a and b, respectively. This implies that the modification of Au NPs can effectively promote the separation and migration of photogenerated carriers in the 0.5 % Au-$ZnGa_2O_4$ sample, leading to enhanced photocatalytic oxidative coupling of CH_4 molecules on the catalyst surface. In addition, the low fluorescence intensity observed for the 0.5 % Au-$ZnGa_2O_4$ sample indicates a significant improvement in the separation efficiency of photogenerated carriers relative to pure $ZnGa_2O_4$, as presented in Fig. 4c. These findings suggest that the modification of Au NPs facilitates the migration and separation of photogenerated carriers, leading to the observed superior photocatalytic performance of the 0.5 % Au-$ZnGa_2O_4$ photocatalyst in the CH_4 oxidative coupling reaction.

3.4. Discussion on the reaction mechanism

Both pure $ZnGa_2O_4$ and $ZnGa_2O_4$ modified with 0.5 % Au NPs demonstrate activity for oxidative coupling of CH_4. However, the

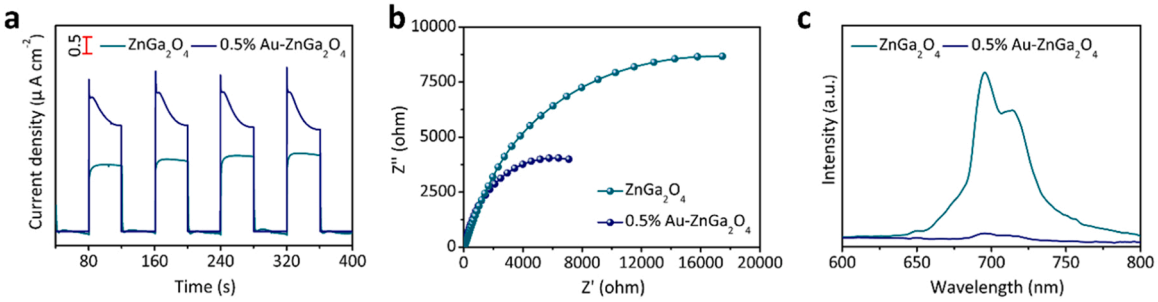

Fig. 4. (a) Electrochemical photocurrents, (b) electrochemical impedance spectra, and (c) photoluminescence spectra of $ZnGa_2O_4$ and 0.5 % Au-$ZnGa_2O_4$ samples.

significant differences in product activity and selectivity between the two samples may correspond to different reaction mechanisms. The CH_4 desorption temperatures of pure $ZnGa_2O_4$ and 0.5 % Au-$ZnGa_2O_4$ samples are consistent, indicating that the chemisorption capacities for CH_4 molecules are similar. The difference in the CH_4 desorption peak at 420 °C only means that the 0.5 % Au-$ZnGa_2O_4$ sample has a higher CH_4 adsorption quantity than pure $ZnGa_2O_4$ (Fig. 5a). Thus, the modification of Au NPs cannot achieve the activation of CH_4 molecules. Instead, the activation of CH_4 molecules may occur on the $ZnGa_2O_4$ support. The TPD test of O_2 shows that the 0.5 % Au-$ZnGa_2O_4$ sample has a better O_2 adsorption ability than $ZnGa_2O_4$, as indicated by the more prominent peak area of the desorption peak of chemisorbed O_2 centered at ~430 °C (Fig. 5b). This suggests that the modification of Au NPs can promote the adsorption and activation of O_2 by $ZnGa_2O_4$. The activated O_2 molecules generate O_2^- to attack the activated CH_4 molecules adsorbed on the surface of $ZnGa_2O_4$, thus realizing the dehydrogenation coupling of CH_4 molecules. In addition, the dehydrogenation of CH_4 molecules to generate $\bullet CH_3$, and the coupling of $\bullet CH_3$ to produce C_2H_6, is a recognized reaction pathway in oxidative coupling of CH_4 [34,35]. Therefore, in situ electron paramagnetic resonance (EPR) spectroscopy is employed to monitor the pathways through which $\bullet CH_3$ may be generated during the reaction. It's worth noting that neither the pure EPR tube nor the injection of Ar into the EPR tube produced any signal (Fig. S8). Fig. 5c shows the EPR spectra of the pure $ZnGa_2O_4$ sample under dark and light conditions in an O_2 atmosphere. In the dark, the $ZnGa_2O_4$ sample shows EPR signals at $g = 1.959$ and 2.002, which are assigned to zinc ions acting as donors and oxygen vacancies, respectively [36,37]. However, under light irradiation, the capture of photogenerated electrons by oxygen vacancies results in the disappearance of the EPR signal. Simultaneously, the signal of zinc ion as a donor is enhanced. Furthermore, a set of EPR signals generated at $g = 2.001$, $g = 2.017$, $g = 2.022$, and $g = 2.031$ is attributed to O_2^-, which is caused by the oxidation of O_2 by photogenerated electrons [38,39]. It is worth noting that the O_2^- may be the critical active species for inducing the generation of $\bullet CH_3$ from CH_4 molecules. In the dark, in the mixed gas of CH_4 and O_2, $ZnGa_2O_4$ still shows signals of zinc ions as donors and oxygen vacancies. However, the signal ascribed to O_2^- is significantly reduced during illumination, as shown in Fig. 5d. This indicates that the CH_4 molecule undergoes a significant chemical reaction with the O_2^-, resulting in a reduction in the concentration of the O_2^- and the production of $\bullet CH_3$. Compared with $ZnGa_2O_4$, the 0.5 % Au-$ZnGa_2O_4$ sample shows a stronger O_2^- signal in the O_2 atmosphere under light conditions, indicating that the modification of Au NPs can promote the adsorption and activation of O_2 (Fig. 5e). Similarly, it was observed that the intensity of O_2^- signal in the mixed atmosphere of CH_4 and O_2 was reduced in the 0.5 % Au-$ZnGa_2O_4$ sample under illumination compared to the EPR signal in the O_2 atmosphere (Fig. 5f). This finding further supports the occurrence of a chemical reaction between CH_4 molecules and O_2^- under light conditions. Therefore, the above results demonstrate that both pure $ZnGa_2O_4$ and Au NPs-modified $ZnGa_2O_4$ are capable of achieving O_2 adsorption and activation. Additionally, the modification of Au NPs can enhance the adsorption and activation capacity of O_2, resulting in the generation

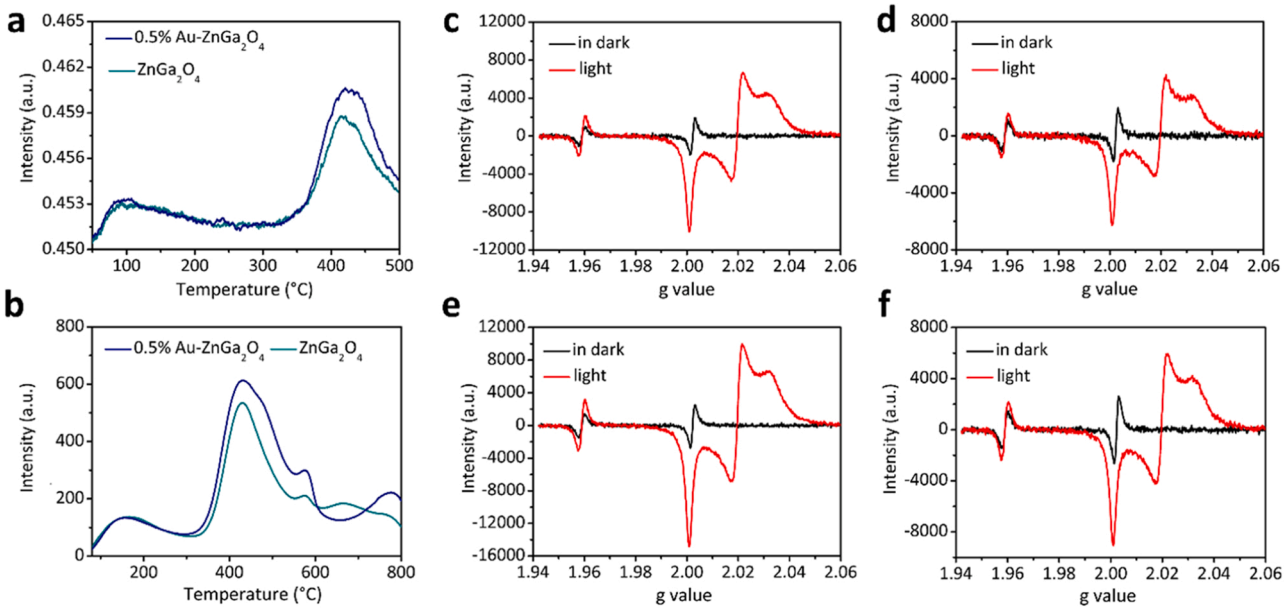

Fig. 5. (a) CH_4-TPD of $ZnGa_2O_4$ and 0.5 % Au-$ZnGa_2O_4$ samples. (b) O_2-TPD of $ZnGa_2O_4$ and 0.5 % Au-$ZnGa_2O_4$ samples. (c) In situ EPR spectra of $ZnGa_2O_4$ in O_2. (d) In situ EPR spectra of $ZnGa_2O_4$ in $CH_4 + O_2$. (e) In situ EPR spectra of 0.5 % Au-$ZnGa_2O_4$ in O_2. (f) In situ EPR spectra of 0.5 % Au-$ZnGa_2O_4$ in $CH_4 + O_2$.

of more O_2^- species that can induce the conversion of CH_4 into $\bullet CH_3$.

The modification of Au NPs not only enhances the adsorption and activation ability of O_2, leading to the production of more O_2^- species, which induces CH_4 to form $\bullet CH_3$, but also efficiently adsorbs and stabilizes $\bullet CH_3$. Therefore, in situ EPR experiments were conducted to detect the signals generated by CH_4 and O_2. The signals of the DMPO-$\bullet CH_3$ integrated object were not detected on the surface of $ZnGa_2O_4$ and 0.5 % Au-$ZnGa_2O_4$ without light irradiation. However, under light conditions, the signals of DMPO-$\bullet CH_3$ were detected on the surface of $ZnGa_2O_4$ and 0.5 % Au-$ZnGa_2O_4$ samples (Fig. 6a). It is worth noting that the signal of DMPO-$\bullet CH_3$ on the surface of 0.5 % Au-$ZnGa_2O_4$ is significantly stronger than that on the surface of $ZnGa_2O_4$ (Fig. 6b). This confirms that the modification of Au NPs can promote the generation and stabilization of $\bullet CH_3$. Furthermore, Both $ZnGa_2O_4$ and 0.5 % Au-$ZnGa_2O_4$ have been shown to effectively adsorb and activate O_2 to generate O_2^-, which in turn attacks CH_4 molecules to produce $\bullet CH_3$. However, on the $ZnGa_2O_4$ surface, most of the $\bullet CH_3$ is converted to CO_2 with only a small amount coupling into C_2H_6. In contrast, 0.5 % Au-$ZnGa_2O_4$ efficiently couples most of the $\bullet CH_3$ into C_2H_6 and only converts a small amount to CO_2. To monitor the catalytic process of this reaction, in situ diffuse reflectance infrared Fourier transform spectroscopy was employed. Fig. 6c displays the infrared Fourier transform spectra of pure $ZnGa_2O_4$ with varying illumination times under the mixed atmosphere of CH_4 and O_2. The infrared absorption peak at 1539 cm^{-1}, assigned to the b-CO_3^{2-} species absorption peak on the catalyst surface, was detected under light conditions [40]. b-CO_3^{2-} is a significant intermediate in the photocatalytic oxidation of CH_4 to CO_2. Furthermore, the infrared absorption peaks at 3014 cm^{-1} and 1302 cm^{-1} are attributed to the infrared absorption peaks of CH_4, which has four vibrational modes: v_1-v_4, with frequencies of 2917, 1533, 3019, and 1306 cm^{-1}, respectively. Among these modes, v_1 and v_2 are infrared-forbidden modes, while v_3 and v_4 are infrared-active modes [41]. In contrast, only the infrared peak at 3014 cm^{-1} is detected on the 0.5 % Au-$ZnGa_2O_4$ sample, and the infrared peak at 1302 cm^{-1} is not detected (Fig. 6d). This suggests that the infrared absorption peak at 1302 cm^{-1}, associated with the v_4 mode, diminishes due to the occupation of surface sites available for CH_4 adsorption by Au NPs. [41] Additionally, the key intermediates for the overoxidation of CH_4 to CO_2 are not detected. This indicates that Au NPs are effective in reducing the excessive oxidation of CH_4 on the surface of $ZnGa_2O_4$.

3.5. Theoretical calculation

The activation and cleavage of CH_4 are initiated by O_2^-. However, bare $ZnGa_2O_4$ without Au generates only a small amount of C_2H_6 and over-oxidizes most of CH_4 to CO_2. Therefore, we believe that Au plays a crucial role in coupling the $\bullet CH_3$ intermediate to C_2H_6 during the reaction. Conversely, if $\bullet CH_3$ is located on the surface of $ZnGa_2O_4$ nanosheets, it will be further oxidized to CO_2. Hence, theoretical calculations were utilized to determine the reaction site for the coupling of $\bullet CH_3$ to C_2H_6. As depicted in Fig. 7, compared with pure $ZnGa_2O_4$ nanosheets, $\bullet CH_3$ adsorption on the surface of Au NPs requires overcoming an energy barrier of 0.45 eV, while adsorption on the surface of $ZnGa_2O_4$

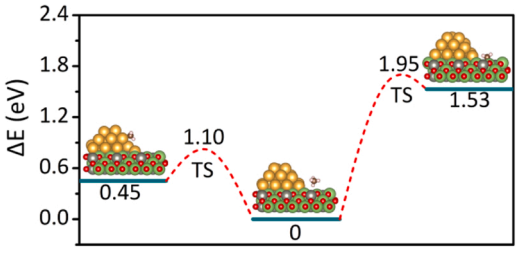

Fig. 7. The energy barrier of C-H bond cleavage of CH_4 on 0.5 % Au-$ZnGa_2O_4$.

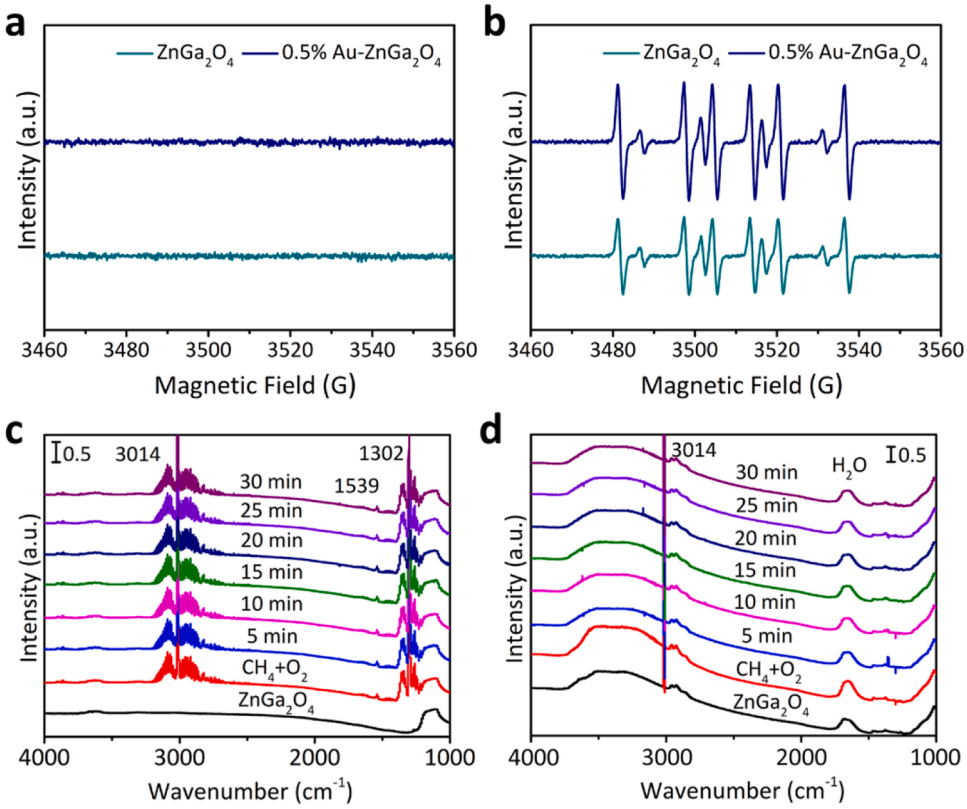

Fig. 6. The EPR spectra are collected in CH_4 and H_2O at room temperature with DMPO as atrapping agent. (a) in the dark. (b) in the light. In situ FTIR spectra for photocatalytic conversion of CH_4 over (c) $ZnGa_2O_4$ and (d) 0.5 % Au-$ZnGa_2O_4$.

necessitates overcoming an energy barrier of 1.53 eV. Obviously, •CH_3 is more readily adsorbed on the surface of Au NPs [11]. Due to the stable adsorption of •CH_3 by Au NPs, •CH_3 is efficiently coupled to C_2H_6 on the surface of Au NPs, and further reaction with O_2^- is avoided. On the contrary, on the $ZnGa_2O_4$ surface, due to the co-existence of •CH_3 and O_2^-, excessive oxidation of •CH_3 to CO_2 occurs, and only a small amount of •CH_3 is coupled to C_2H_6.

Based on the preceding discussion, we propose a reaction mechanism for the photocatalytic coupling of CH_4 into C_2H_6 on the 0.5 % Au-$ZnGa_2O_4$ sample, as shown in Eqs. 1–7. First, under light conditions, 0.5 % Au-$ZnGa_2O_4$ is excited to generate photogenerated electrons and holes. The photogenerated electrons are annihilated by oxygen vacancies, resulting in the disappearance of the oxygen vacancy signal. However, photogenerated electrons can reduce the O_2 adsorbed on the sample surface to O_2^-. As an important active species, O_2^- is further reduced to O^- by photogenerated electrons [42,43]. O^- is used for the extraction of H^+ in CH_4, resulting in •CH_3 and OH^-. Finally, •CH_3 is coupled on the surface of Au NPs to generate C_2H_6 and desorbed, while OH^- is transformed into O^{2-} and placed in 0.5 % Au-$ZnGa_2O_4$ crystals to form lattice oxygen.

$$Zn^{2+}[Ga_2^{3+}O_3^{2-}V_O^{'}] \longrightarrow^{hv} Zn^{2+}[Ga_2^{3+}O_3^{2-}V_O] + 2e^- \quad (1)$$

$$O_2 + e^- \rightarrow O_2^- \quad (2)$$

$$O_2^- + e^- \rightarrow 2O^- \quad (3)$$

$$2\,CH_4 + 2O^- \rightarrow 2CH_3\cdot + 2OH^- \quad (4)$$

$$2OH^- \rightarrow O^{2-} + H_2O \quad (5)$$

$$Zn^{2+}[Ga_2^{3+}O_3^{2-}V_O] + O^{2-} \rightarrow Zn^{2+}[Ga_2^{3+}O_4^{2-}] \quad (6)$$

$$2CH_3\cdot \longrightarrow^{Au} C_2H_6 \quad (7)$$

4. Conclusions

In summary, we report the successful preparation of $ZnGa_2O_4$ nanosheet photocatalysts using a one-step solvothermal method, followed by surface modification with Au NPs via a simple chemical reduction approach. The resulting noble metal-modified inorganic semiconductor photocatalysts demonstrate unique catalytic effects on the oxidative coupling of CH_4 under full-band irradiation. The presence of Au NPs promotes the adsorption and activation of O_2, resulting in the generation of O_2^-, which in turn facilitates the cracking of CH_4 into •CH_3 and its subsequent coupling into C_2H_6. Moreover, Au NPs are effective in stabilizing •CH_3 and preventing its excessive oxidation to CO_2. As a result, the optimal Au NPs modified $ZnGa_2O_4$ photocatalyst exhibits a C_2H_6 yield of 1315.3 μmol g^{-1} h^{-1} and a selectivity of 53 %, both of which are significantly higher than those of pure $ZnGa_2O_4$. Our findings are supported by both photoelectrochemical and fluorescence measurements, which indicate that the modification of Au NPs promotes the separation and migration of photogenerated charges, thereby enhancing CH_4 conversion. In addition to providing a feasible process for CH_4 resource conversion, this work can serve as a landmark achievement in the field of solar energy.

CRediT authorship contribution statement

Yao Chai: Experimental data analysis and writing. **Sishi Tang:** Catalyst preparation, performance testing and characterization. **Qiang Wang:** Catalyst preparation, performance testing and characterization. **Qiong Wu:** Catalyst performance testing. **Jun Liang:** Writing review & editing. **Li Li:** Experimental design and editing.

Declaration of Competing Interest

The authors declare that they have no known competing financial interests or personal relationships that could have appeared to influence the work reported in this paper.

Data Availability

Data will be made available on request.

Acknowledgements

This research was financially supported by the Key Project of Natural Science Foundation of Ningxia (2023AAC0200X, 2023AAC02002) and the National Natural Science Foundation of China (Grant Nos. 21862015, 21865022).

Appendix A. Supporting information

Supplementary data associated with this article can be found in the online version at doi:10.1016/j.apcatb.2023.123012.

References

[1] H. Song, X. Meng, S. Wang, W. Zhou, S. Song, T. Kako, J. Ye, Selective photooxidation of methane to methanol with oxygen over dual-cocatalyst-modified titanium dioxide, ACS Catal. 10 (2020) 14318–14326, https://doi.org/10.1021/acscatal.0c04329.

[2] H. Song, X. Meng, S. Wang, W. Zhou, X. Wang, T. Kako, J. Ye, Direct and selective photocatalytic oxidation of CH_4 to oxygenates with O_2 on cocatalysts/ZnO at room temperature in water, J. Am. Chem. Soc. 141 (2019) 20507–20515, https://doi.org/10.1021/jacs.9b11440.

[3] J. Xie, R. Jin, A. Li, Y. Bi, Q. Ruan, Y. Deng, Y. Zhang, S. Yao, G. Sankar, D. Ma, J. Tang, Highly selective oxidation of methane to methanol at ambient conditions by titanium dioxide-supported iron species, Nat. Catal. 1 (2018) 889–896 (https://doi.org/).

[4] N. Agarwal, S.J. Freakley, R.U. McVicker, S.M. Althahban, N. Dimitratos, Q. He, D. J. Morgan, R.L. Jenkins, D.J. Willock, S.H. Taylor, C.J. Kiely, G.J. Hutchings, Aqueous Au-Pd colloids catalyze selective CH_4 oxidation to CH_3OH with O_2 under mild conditions, Science 358 (2017) 223–227, https://doi.org/10.1126/science.aan6515.

[5] J. Shan, M. Li, L.F. Allard, S. Lee, M. Flytzani-Stephanopoulos, Mild oxidation of methane to methanol or acetic acid on supported isolated rhodium catalysts, Nature 551 (2017) 605–608, https://doi.org/10.1038/nature24640.

[6] Z. Jin, L. Wang, E. Zuidema, K. Mondal, M. Zhang, J. Zhang, C. Wang, X. Meng, H. Yang, C. Mesters, F.-S. Xiao, Hydrophobic zeolite modification for in situ peroxide formation in methane oxidation to methanol, Science 367 (2020) 193–197, https://doi.org/10.1126/science.aaw1108.

[7] H. Song, X. Meng, Z.-j Wang, H. Liu, J. Ye, Solar-energy-mediated methane conversion, Joule (3) (2019) 1606–1636, https://doi.org/10.1016/j.joule.2019.06.023.

[8] Z. Zuo, P.J. Ramirez, S. Senanayake, P. Liu, J.A. Rodriguez, The low-temperature conversion of methane to methanol on CeO_x/Cu_2O catalysts: water controlled activation of the C−H bond, J. Am. Chem. Soc. 138 (2016) 13810–13813, https://doi.org/10.1021/jacs.6b08668.

[9] S.D. Angeli, G. Monteleone, A. Giaconia, A.A. Lemonidou, State-of-the-art catalysts for CH4 steam reforming at low temperature, Int. J. Hydrogen Energy 39 (2014) 1979–1997, https://doi.org/10.1016/j.ijhydene.2013.12.001.

[10] K. Villa, S. Murcia-López, J.R. Morante, T. Andreu, An insight on the role of La in mesoporous WO_3 for the photocatalytic conversion of methane into methanol, Appl. Catal. B 187 (2016) 30–36, https://doi.org/10.1016/j.apcatb.2016.01.032.

[11] S. Song, H. Song, L. Li, S. Wang, W. Chu, K. Peng, X. Meng, Q. Wang, B. Deng, Q. Liu, Z. Wang, Y. Weng, H. Hu, H. Lin, T. Kako, J. Ye, A selective Au-ZnO/TiO_2 hybrid photocatalyst for oxidative coupling of methane to ethane with dioxygen, Nat. Catal. 4 (2021) 1032–1042, https://doi.org/10.1038/s41929-021-00708-9.

[12] L. Meng, Z. Chen, Z. Ma, S. He, Y. Hou, H.-H. Li, R. Yuan, X.-H. Huang, X. Wang, X. Wang, J. Long, Gold plasmon-induced photocatalytic dehydrogenative coupling of methane to ethane on polar oxide surfaces, Energy Environ. Sci. 11 (2018) 294–298, https://doi.org/10.1039/c7ee02951a.

[13] W. Zhang, C. Fu, J. Low, D. Duan, J. Ma, W. Jiang, Y. Chen, H. Liu, Z. Qi, R. Long, Y. Yao, X. Li, H. Zhang, Z. Liu, J. Yang, Z. Zou, Y. Xiong, High-performance photocatalytic nonoxidative conversion of methane to ethane and hydrogen by heteroatoms-engineered TiO_2, Nat. Commun. 13 (2022) 2806, https://doi.org/10.1038/s41467-022-30532-z.

[14] S. Wu, X. Tan, J. Lei, H. Chen, L. Wang, J. Zhang, Ga-doped and Pt-loaded porous TiO2-SiO2 for photocatalytic nonoxidative coupling of methane, J. Am. Chem. Soc. 141 (2019) 6592–6600, https://doi.org/10.1021/jacs.8b13858.

[15] Z. Chen, S. Wu, J. Ma, S. Mine, T. Toyao, M. Matsuoka, L. Wang, J. Zhang, Non-oxidative coupling of methane: N-type doping of niobium single atoms in

TiO_2−SiO_2 induces electron localization, Angew. Chem. Int. Ed. 133 (2021) 12008–12016, https://doi.org/10.1002/anie.202016420.
[16] L. Luo, Z. Gong, Y. Xu, J. Ma, H. Liu, J. Xing, J. Tang, Binary Au−Cu reaction sites decorated ZnO for selective methane oxidation to C1 oxygenates with nearly 100 % selectivity at room temperature, J. Am. Chem. Soc. 144 (2022) 740–750, https://doi.org/10.1021/jacs.1c09141.
[17] P. Schwach, X. Pan, X. Bao, Direct conversion of methane to value-added chemicals over heterogeneous catalysts: challenges and prospects, Chem. Rev. 117 (2017) 8497–8520, https://doi.org/10.1021/acs.chemrev.6b00715.
[18] L. Li, S. Fan, X. Mu, Z. Mi, C.-J. Li, Photoinduced conversion of methane into benzene over GaN nanowires, J. Am. Chem. Soc. 136 (2014) 7793–7796, https://doi.org/10.1021/ja5004119.
[19] L. Yuliati, H. Yoshida, Photocatalytic conversion of methane, Chem. Soc. Rev. (37) (2008) 1592–1602, https://doi.org/10.1039/b710575b.
[20] S. Zhu, X. Li, Z. Pan, X. Jiao, K. Zheng, L. Li, W. Shao, X. Zu, J. Hu, J. Zhu, Y. Sun, Y. Xie, Efficient photooxidation of methane to liquid oxygenates over ZnO nanosheets at atmospheric pressure and near room temperature, Nano Lett. 21 (2021) 4122–4128, https://doi.org/10.1021/acs.nanolett.1c01204.
[21] Q. Liu, D. Wu, Y. Zhou, H. Su, R. Wang, C. Zhang, S. Yan, M. Xiao, Z. Zou, Single-crystalline, ultrathin $ZnGa_2O_4$ nanosheet scaffolds to promote photocatalytic activity in CO_2 reduction into methane, ACS Appl. Mater. Interfaces 6 (2014) 2356–2361, https://doi.org/10.1021/am404572g.
[22] J. Liang, Y. Chai, L. Li, D. Li, J. Shen, Y. Zhang, X. Wang, Germanium and iron double-substituted $ZnGa_2O_4$ solid-solution photocatalysts with modulated band structure for boosting photocatalytic CO_2 reduction with H_2O, Appl. Catal., B 265 (2020), 118551, https://doi.org/10.1016/j.apcatb.2019.118551.
[23] X. Zheng, X. Yan, J. Ma, X. Yao, J. Zhang, L. Wang, Unidirectional/bidirectional electron transfer at the Au/TiO_2 interface operando tracked by SERS spectra from Au and TiO_2, ACS Appl. Mater. Interfaces 13 (2021 1649) 8–16506, https://doi.org/10.1021/acsami.1c02540.
[24] Y. Cao, L. Guo, M. Dan, D.E. Doronkin, C. Han, Z. Rao, Y. Liu, J. Meng, Z. Huang, K. Zheng, P. Chen, F. Dong, Y. Zhou, Modulating electron density of vacancy site by single Au atom for effective CO_2 photoreduction, Nat. Commun. (12) (2021) 1675, https://doi.org/10.1038/s41467-021-21925-7.
[25] M.-Y. Lu, X. Zhou, C.-Y. Chiu, S. Crawford, S. Gradecak, From GaN to $ZnGa_2O_4$ through a low-temperature process: nanotube and heterostructure arrays, ACS Appl. Mater. Interfaces 6 (2014) 882–887, https://doi.org/10.1021/am404158f.
[26] P.-H. Huang, Y.-C. Shen, C.-Y. Tung, C.-Y. Huang, C.S. Tan, R.-H. Horng, Energy-saving $ZnGa_2O_4$ phototransistor improved by thermal annealing, ACS Appl. Electron. Mater. 2 (2020) 3515–3521, https://doi.org/10.1021/acsaelm.0c00394.
[27] L.-C. Cheng, M.-R. Wu, C.-Y. Huang, T.-K. Juang, P.-L. Liu, R.-H. Horng, Effect of defects on the properties of $ZnGa_2O_4$ thin-film transistors, ACS Appl. Electron. Mater. 1 (2019) 253–259, https://doi.org/10.1021/acsaelm.8b00093.
[28] M. Zhao, Y. Gu, P. Chen, Z. Xin, H. Zhu, B. Wang, K. Zhu, S. Yan, Z. Zou, Highly selective electrochemical CO_2 reduction to CO using a redox-active couple on low-crystallinity mesoporous $ZnGa_2O_4$ catalyst, J. Mater. Chem. A 7 (2019) 9316–9323, https://doi.org/10.1039/c9ta00562e.
[29] J.-J. Li, B.-L. Zhu, G.-C. Wang, Z.-F. Liu, W.-P. Huang, S.-M. Zhang, Enhanced CO catalytic oxidation over an Au–Pt alloy supported on TiO_2 nanotubes: investigation of the hydroxyl and Au/Pt ratio influences, Catal. Sci. Technol. 8 (2018) 6109–6122, https://doi.org/10.1039/c8cy01642a.
[30] K. Zhang, G. Lu, F. Chu, X. Huang, Au/TiO_2 nanobelts: thermal enhancement vs. plasmon enhancement for visible-light-driven photocatalytic selective oxidation of amines into imines, Catal. Sci. Technol. 11 (2021) 7060–7071, https://doi.org/10.1039/d1cy01333e.
[31] P. Bai, X. Zhao, W.L. Fan, Preparation and enhanced photocatalytic hydrogen-evolution activity of $ZnGa_2O_4$/N-rGO heterostructures, RSC Adv. 7 (2017) 53145–53156, https://doi.org/10.1039/c7ra09981a.
[32] R.M. Palomino, R.A. Gutiérrez, Z. Liu, S. Tenney, D.C. Grinter, E. Crumlin, I. Waluyo, P.J. Ramírez, J.A. Rodriguez, S.D. Senanayake, Inverse catalysts for CO oxidation: enhanced oxide–metal interactions in MgO/Au (111), CeO_2/Au (111), and TiO_2/Au (111), ACS Sustain. Chem. Eng. 5 (2017) 10783–10791, https://doi.org/10.1021/acssuschemeng.7b02744.
[33] Y. Chai, Y. Chen, J. Shen, M. Ni, B. Wang, D. Li, Z. Zhang, X. Wang, Distortion of the coordination structure and high symmetry of the crystal structure in In_4SnS_8 microflowers for enhancing visible-light photocatalytic CO_2 reduction, ACS Catal. 11 (2021) 11029–11039, https://doi.org/10.1021/acscatal.1c02937.
[34] Y. Wang, P. Hu, J. Yang, Y. Zhu, D. Chen, C–H bond activation in light alkanes: a theoretical perspective, Chem. Soc. Rev. 50 (2021) 4299–4358, https://doi.org/10.1039/d0cs01262a.
[35] X. Li, C. Wang, J. Tang, Methane transformation by photocatalysis, Nat. Rev. Mater. 7 (2022) 617–632, https://doi.org/10.1038/s41578-022-00422-3.
[36] E. Morra, G. Berlier, E. Borfecchia, S. Bordiga, P. Beato, M. Chiesa, Electronic and geometrical structure of Zn^+ ions stabilized in the porous structure of Zn-loaded zeolite H-ZSM-5: a multifrequency CW and pulse EPR study, J. Phys. Chem. C. 121 (2017) 14238–14245, https://doi.org/10.1021/acs.jpcc.7b04289.
[37] G. Wu, J. Zhao, X. Sun, Y. Cao, J. He, Li.D. Feng, The effect of oxygen vacancies in ZnO at an Au/ZnO interface on its catalytic selective oxidation of glycerol, J. Catal. 377 (2019) 271–282, https://doi.org/10.1016/j.jcat.2019.06.030.
[38] J.B. Priebe, J. Radnik, A.J.J. Lennox, M.-M. Pohl, M. Karnahl, D. Hollmann, K. Grabow, U. Bentrup, H. Junge, M. Beller, A. Brückner, Solar hydrogen production by plasmoni Au-TiO2 catalysts: impact of synthesis protocol and TiO2 phase on charge transfer efficiency and H2 evolution rates, ACS Catal. 5 (2015) 2137–2148, https://doi.org/10.1021/cs5018375.
[39] R.F. Howe, M. Gratzel, EPR study of hydrated anatase under UV irradiation, J. Phys. Chem. 91 (1987) 3906–3909, https://doi.org/10.1021/j100298a035.
[40] Y. Liu, D. Shen, Q. Zhang, Y. Lin, F. Peng, Enhanced photocatalytic CO_2 reduction in H_2O vapor by atomically thin Bi_2WO_6 nanosheets with hydrophobic and nonpolar surface, Appl. Catal., B (283 (2021), 119630, https://doi.org/10.1016/j.apcatb.2020.119630.
[41] C. Li, Q. Xin, FT-IR spectroscopic investigation of methane adsorption on cerium oxide, J. Phys. Chem. 96 (1992) 7714–7718, https://doi.org/10.1021/j100198a042.
[42] C.-H. Lin, K.D. Campbell, J.-X. Wang, J.H. Lunsford, Oxidative dimerization of methane over lanthanum oxide, J. Phys. Chem. 90 (1986) 534–537, https://doi.org/10.1021/j100276a004.
[43] A.M. Maitra, Critical performance evaluation of catalysts and mechanistic implications for oxidative coupling of methane, Appl. Catal. A-Gen. 104 (1993) 11–59, https://doi.org/10.1016/0926-860X(93)80209-9.